A water transport system across the mantle transition zone beneath western North America as imaged by electrical conductivity data

Shiwen Li, Yabin Li, Junhao Guo, Zikun Zhou, Aihua Weng*
College of Geo-exploration Science and Technology, Jilin University, Changchun 130026, China
*E-mail: wengah@jlu.edu.cn

Supplemental Material

Methods, supplementary table, supplementary figures

Methods
Supplementary Table S1
Supplementary Figure S1
Supplementary Figure S2
Supplementary Figure S3
Supplementary Figure S4
Supplementary Figure S5
Supplementary Figure S6
Supplementary Figure S7
Supplementary Figure S8
Supplementary Figure S9
Supplementary References

METHODS

Data processing and 3D inversion. The geomagnetic depth sounding (GDS) method can link the electrical conductivity around the mantle transition zone (MTZ) with the observed slowly varying geomagnetic fields on Earth's surface (Kelbert et al., 2009) by the *C*-response (Banks, 1969). *C*-response of a certain period/frequency (ω) can be calculated by the vertical ($\mathbf{Z}(\omega)$) and horizontal ($\mathbf{H}(\omega)$) component of magnetic field in geomagnetic spherical coordinates by the following form

$$C(\omega) = -\frac{a\tan\theta}{2}\frac{\mathbf{Z}(\omega)}{\mathbf{H}(\omega)}, \qquad (1)$$

in which a is the radius of Earth and θ is colatitude (0-180°). Squared coherence (coh^2) of $\mathbf{Z}$ and $\mathbf{H}$ is regularly treated as a quality indicator of *C*-response, which can detect those sites with large signal-to-noise ratios (Semenov and Kuvshinov, 2012). The coh^2 is calculated by

$$\mathrm{coh}^2 = \frac{|\sum ZWH^*|^2}{\sum ZWZ^* \sum HWH^*}, \qquad (2)$$

and used to select data (Semenov and Kuvshinov, 2012). Operator * is the complex conjugate and W is an iterative robust weight matrix (Semenov and Kuvshinov, 2012). To estimate *C*-responses from observed geomagnetic fields, the bounded influence remote reference processing (BIRRP) method (Chave and Thomson, 2004) based on self-referenced technology (Semenov and Kuvshinov, 2012) is used. 12 stations located in mid-latitude (Kelbert et al., 2009; Semenov and Kuvshinov, 2012; Li et al., 2020) near our research area (Tab. S1) are selected for data processing (the geomagnetic data is downloaded from World Data Centre). We rescan the observed data, discard noisy segments and reprocess to obtain *C*-responses sampled at 16 periods distributed within the range from 3.56 days to 113.8 days (Li et al., 2020), and the good quality of data is characterized by the smoothness of responses curve in the whole period range (Fig. S1). However, stations like NEW, VIC, SBL, STJ and SJG have a low coh^2 (Fig. S2), indicating poor data quality or unstable responses. Therefore, the contribution from these stations to inversion is reduced by assigning very small weights to the responses to suppress their contribution to the inversion and guarantee the reliability of inversion results.

An L_1-norm regularization 3D inversion algorithm (Li et al., 2020) is used to convert the observed *C*-responses to the electrical conductivity of the mantle of spherical Earth. This method has advantage on avoiding overfitting the outlies and inducing false structures in inversion (Menke, 1984; Farquharson, 2008; Li et al., 2020). The limited-memory quasi-Newton method (L-BFGS) is used to search the optimal solution of the inversion objective functional (Avdeev and Avdeeva, 2009; Kuvshinov and Semenov, 2012; Li et al., 2020), based on a staggered-grid finite difference method for computing the electromagnetic induction *C*-response in spherical coordinates (Uyeshima and Schultz, 2000).

During our inversion, Earth is divided into 12 spherical layers in the radial direction above the core (0-2890 km) (Kelbert et al., 2009). A smoothing strategy is used to balance the conductivity jumps between neighboring grid cells. At the phase transition boundaries (410, 520 and 660 km), model conductivity is allowed to jump (Kelbert et al., 2009). Due to the large conductance diversity between ocean and land, which largely influences the geomagnetic field, a heterogeneous conductive surface layer with a thickness of 12.65 km is set to correct the ocean induction effect (OIE) (Kuvshinov, 2002; Kelbert et al., 2009). Benefiting from the denser stations in the United States, we discretize the conductivity in the spherical shell of Earth (Kelbert et al., 2009) onto homogeneous grids (5° × 5°). Relying on the finer grids (5° × 5°) than previous studies (about 10° × 10°) (Kelbert et al., 2009; Semenov and Kuvshinov, 2012; Li et al., 2020), we can obtain a robust 3D electrical image with a resolution of approximately 10° × 10° near the MTZ that can better resolve the conductivity variation beneath the study area (Fig. S3-S5).

Robustness tests. The high quality of our inversion for preferred model is shown in Fig. 1A and Fig. S1. Strict numerical experiments using the model perturbation method (Burd et al., 2014) are arranged to test the robustness of the two prominent anomalies in the lower MTZ and uppermost lower mantle. We change the electrical conductivity of the anomaly to the starting value and recalculate new model responses. Comparing with those from the preferred model shows obvious deviations in the *C*-responses, implying that these anomalies are robustly delineated (Fig. S6a for anomaly W, Fig. S6b for anomaly E, and Fig. S6c for anomalies W and E). As anomaly W is the core of this work, we also use the fixed model inversion (Li et al., 2020) method to verify its robustness (Fig. S7, S8). The re-inverted conductivity structure around anomaly W deforms to meet the requirement of achieving good data fitting by new inversion, indicating that the erased structure is necessary.

Bulk conductivity in the lower mantle transition zone. The electrical conductivity of the lower MTZ is determined mainly by the conductive mineral ringwoodite. As suggested by Karato (Karato, 2011), the conductivity of a mineral is caused the hopping of electrons between ferric and ferrous iron or the migration of protons, such that the electrical conductivity can be expressed as follows:

$$\sigma = A_1 \cdot f_{O_2}^{q_1}(P,T) \cdot exp\left(-\frac{H_1^*}{RT}\right) + A_2 \cdot f_{O_2}^{q_2}(P,T) \cdot C_W^r \cdot exp\left(-\frac{H_2^*(C_W)}{RT}\right), \qquad (3)$$

where A_1 and A_2 are the pre-exponential terms, f_{O_2} is the oxygen fugacity, q_1 and q_2 are the oxygen fugacity exponents, C_W is the water content, r is a constant that depends on the mechanism of electrical conduction, and H_1^* and H_2^* are the activation enthalpies.

According to equation (3), the electrical conductivity (σ) of ringwoodite can be calculated from the oxygen fugacity and water content, as shown in Fig. S9a.

Mineral compositions of the subducting slab in the topmost lower mantle. In the P-T condition of the topmost lower mantle, materials in subducting crust (20 vol.% of the subducting slab) may have converted to liebermannite (Lib) (35 vol.% of crustal slab), stishovite (Stv) (25 vol.% of crustal slab) and other minerals like majorite garnet (Mj) (40 vol.% of crustal slab) (Yoshino et al., 2014; Lin et al., 2019; Manthilake et al., 2020). The dense hydrous magnesium silicates (DHMSs) in the crust have transitioned to bridgmanite (Brg) because the temperature in the warm Farallon slab has exceeded their stability boundary. These Brg and those transformed from lithospheric mantle of the slab after passing through 660 km interface occupy about 80 vol.% of the slab. Therefore, in the topmost lower mantle, the volume percent of main minerals in the slab are Lib 7% (35 vol.% × 20 vol.%), Stv 5% (25 vol.% × 20 vol.%), Mj 8% (40 vol.% × 20 vol.%), and Brg 80 vol.%, respectively.

Bulk conductivity in the lower mantle. The electrical conductivity for the main minerals of slab are *P-T-X* function (Yoshino et al., 2008b, 2008a, 2014), but pressure effect could be ignored (Yoshino, 2010; Karato and Wang, 2013). We apply the simplified models as first-order approximation to calculate the bulk conductivity of the slab in the uppermost lower mantle. Due to the water capacity of Brg is rather small, the conductivity of dry Brg is calculated based on the measurements of Sinmyo et al. (Sinmyo et al., 2014), which is approximately 1 S/m. In the relatively cold conditions (1600 K) of the slab (Fig. 1d) compared with the ambient mantle, conductivity of Mj which is almost dry as well, is mainly determined by temperature but very low (0.01 Sm^{-1}; Yoshino et al., 2008b), and thus could be ignored. The conductivity of Lib (0.1 wt.%) is approximately 0.25 Sm^{-1} (Manthilake et al., 2020). The electrical conductivity of hydrous stishovite is calculated after (Yoshino et al., 2014) (Fig. S9b). The bulk conductivity is calculated using the Hashin-Shtrikman upper-bound (HS+) mixing model (Hashin and Shtrikman, 1962; Ni et al., 2011) from the individual conductivity of Brg, Lib, Stv and their respective volume fractions (80 vol.%, 7 vol.% and 5 vol.% in slab). Accordingly, $\sigma_{bulk} = \sigma_{Lib}(=0.25\ Sm^{-1} \times 7\ vol.\%) + \sigma_{Brg}(=1\ Sm^{-1} \times 80\ vol.\%) + \sigma_{Stv}(=x\ Sm^{-1} \times 5\ vol.\%)$ (Fig. 2b). The average bulk conductivity of anomaly W indicates an approximate 4.5 wt.% water in the stishovites. As water is contained mainly in the stishovites and liebermannites, the average water content in anomaly W is only ~0.23 wt.% (2300 ppm) (4.5 wt.%* 5 vol.% + 0.1 wt.%* 7 vol.%).

Notably, in above models, we did not consider higher water content in liebermannite. More water could enhance its conductivity more significantly than stishovite (Manthilake et al., 2020), but no related data is measured till now to our knowledge. Therefore, the water contents estimated in this study may be the up limit of the actual slab.

Table S1. Station details of the observatories used in this article. GM corresponds to the geomagnetic coordinates, and the data length is the duration of the recorded time-series geomagnetic field data at the station. The time-series geomagnetic field data can be downloaded from the World data centre, http://www.wdc.bgs.ac.uk/.

Code	Station	Latitude	Longitude	GM Latitude	GM Longitude	Data length
BOU	Boulder	40.13	254.76	48.4	320.59	1967-2019
BSL	Bay St. Louis	30.35	270.37	40.05	339.79	1986-2019
DAL	Dallas	32.99	263.25	42.05	331.62	1964-1974
DLR	Del Rio	29.49	259.08	38.3	327.31	1982-2008
FRD	Fredericksburg	38.2	282.63	48.4	353.38	1957-2019
FRN	Fresno	37.09	240.28	43.52	305.25	1982-2020
NEW	Newport	48.27	242.88	54.8	304.93	1966-2019
SBL	Sable Island	43.93	299.99	53.81	14.51	2000-2018
SJG	San Juan	18.11	293.85	28.31	6.08	1967-2017
STJ	Saint Johns	47.60	307.32	57.03	24.03	1968-2019
TUC	Tucson	32.17	249.27	39.88	316.11	1909-2019
VIC	Victoria	48.52	236.58	54.1	297.82	1957-2018

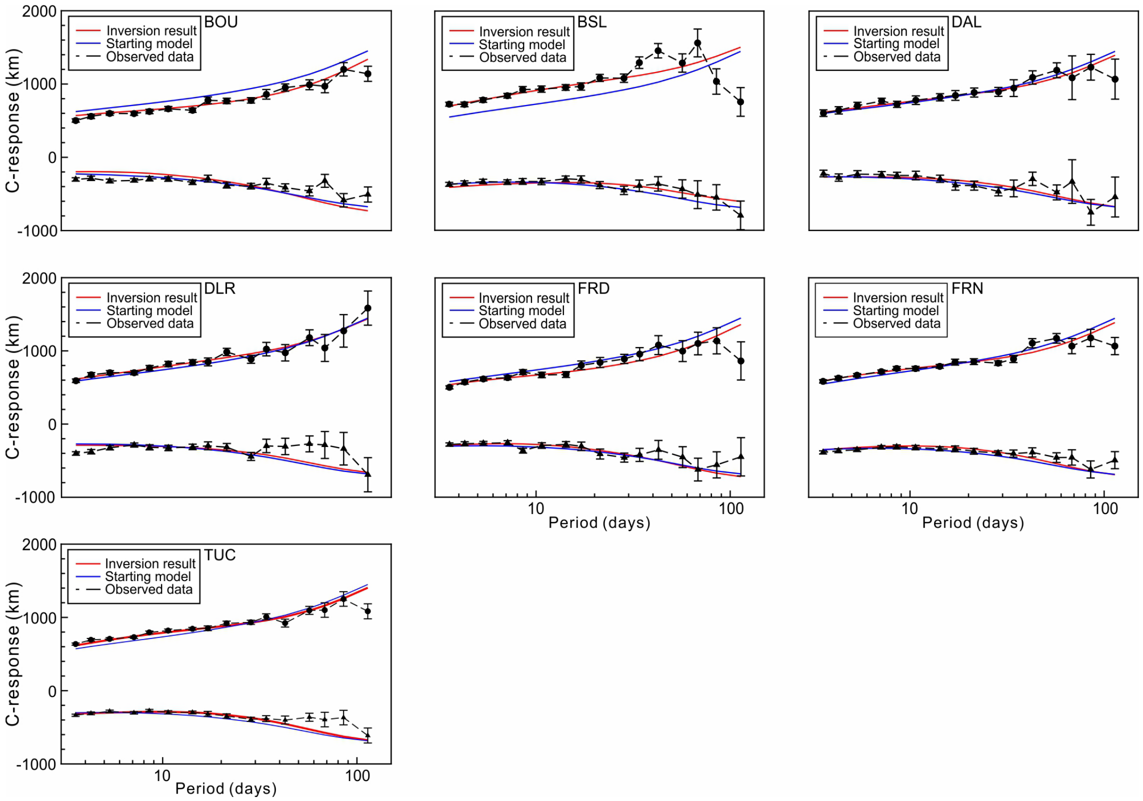

Figure S1. *C*-responses and their data fittings. The responses of the starting model (blue solid lines), inversion result (red solid lines) and observed data (black dashed lines) are drawn for the 7 stations with good quality (Fig. S2). The vertical and short bars represent the data misfit at a certain period.

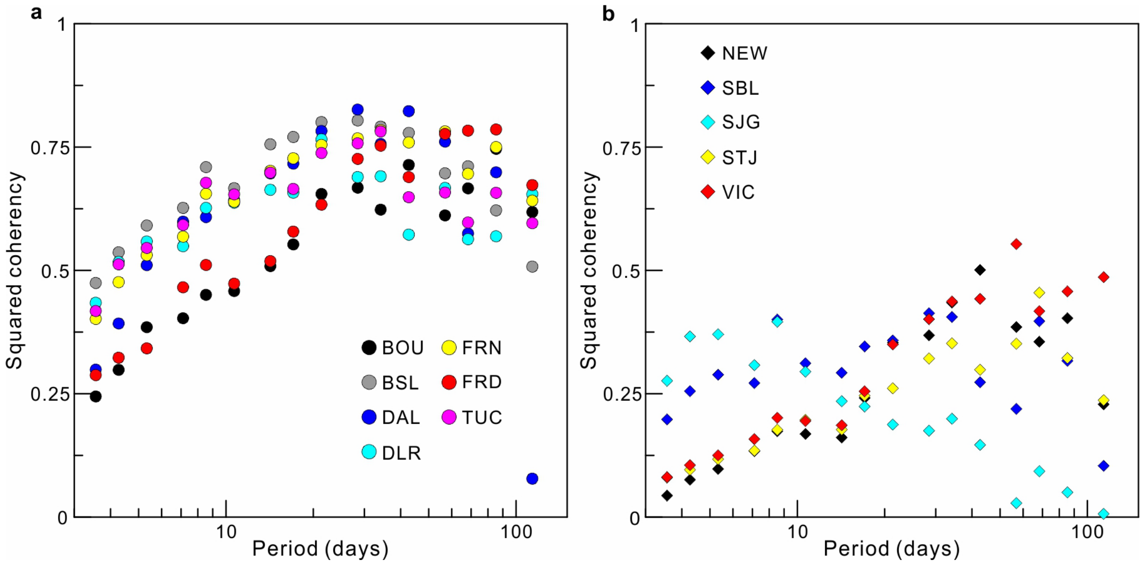

Figure S2. The squared coherencies of Z (vertical component of magnetic field) and H (horizontal component of magnetic field) at 12 selected stations. Stations with relatively high (a) and low (b) squared coherencies corresponding to *C*-response with good (>0.5) and poor (<0.5) quality are shown.

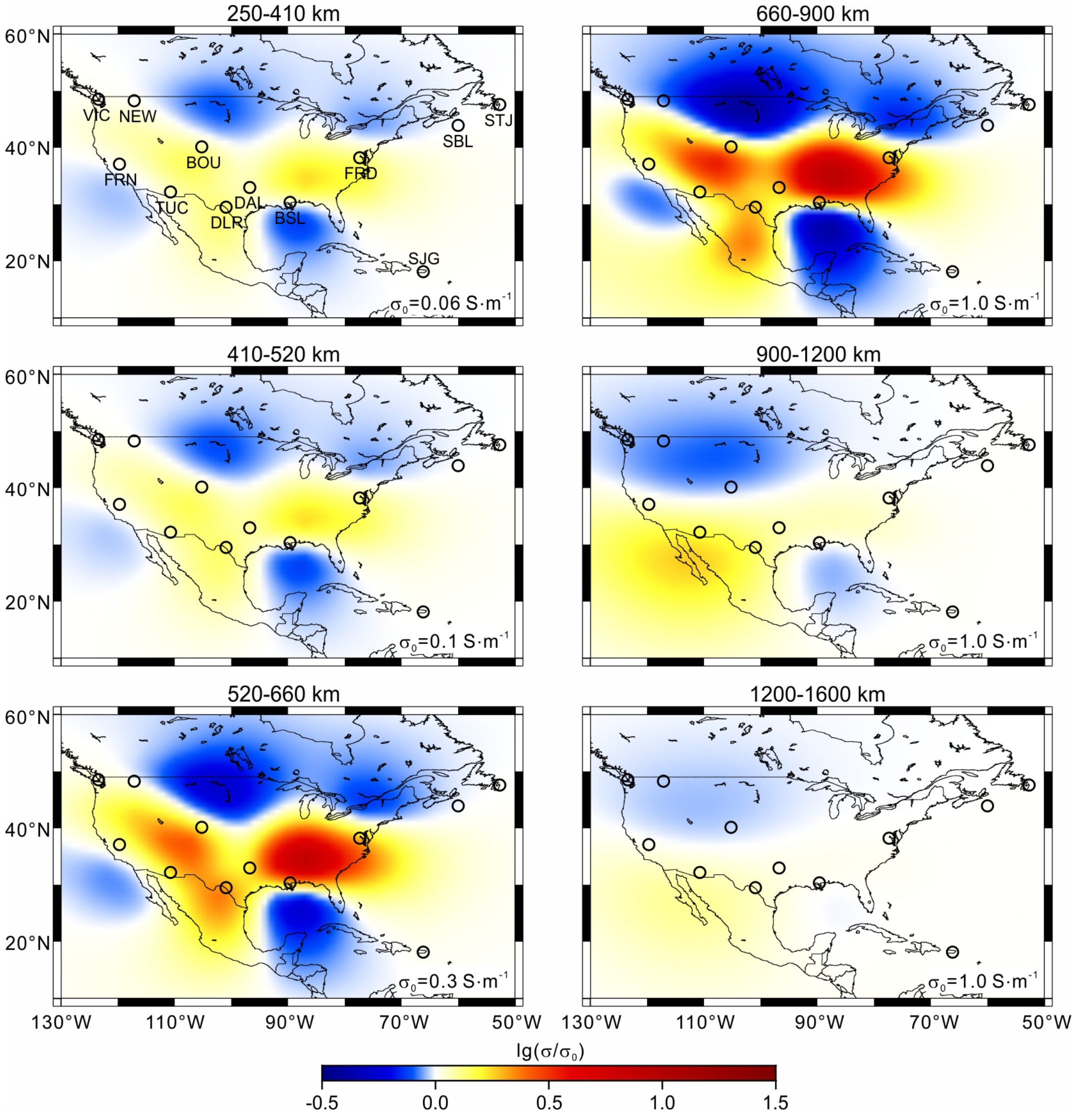

Figure S3. Variations in electrical conductivity at depths of 250-1600 km. Variables $\boldsymbol{\sigma}$ and $\boldsymbol{\sigma_0}$ are the conductivities of the inverted and reference models, respectively.

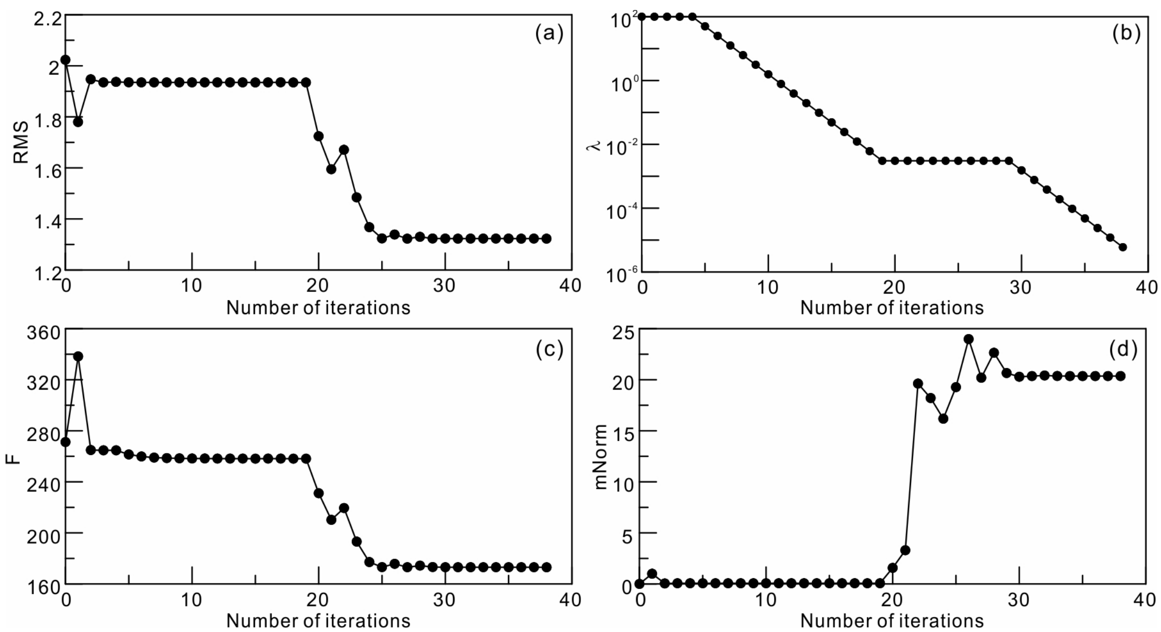

Figure S4. Variations in the data fitting error (shown as root mean square of the misfit (RMS)), regularization parameter (λ), value of penalty function (F) and model correction (mNorm) during inversion of the preferred model. The model correction toward the end of inversion approaches a constant, which means that more iterations of inversion could not change the model conductivity. Meanwhile, the reduction in the regularization parameter cannot increase data fitting, which approaches a constant at the end of inversion and means the inversion have reached a good data fitting.

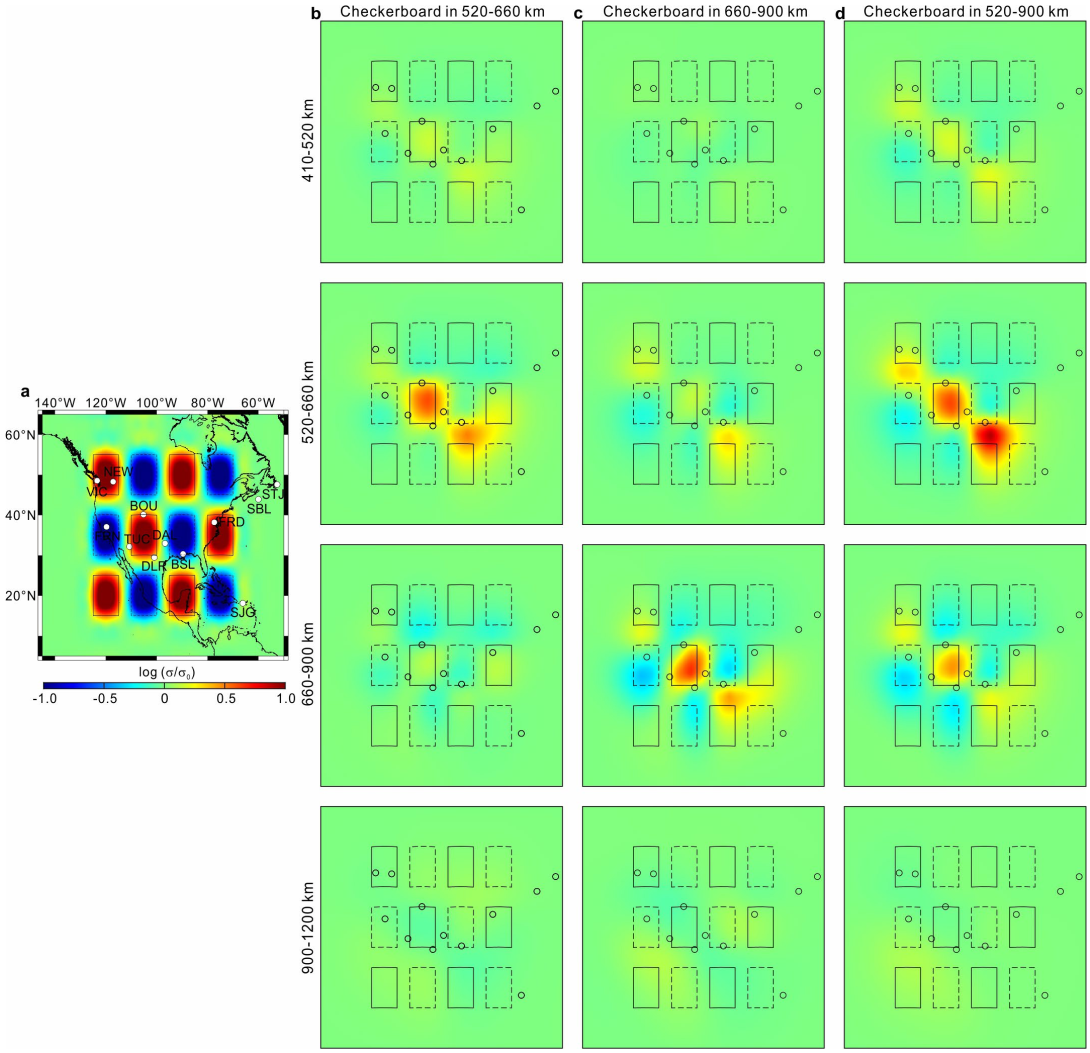

Figure S5. Checkerboard resolution tests. We use the realistic observations distribution in North America. (a) Checkerboard model. The conductivity and resistivity anomalies are ten times higher or lower than those of the 1D average model. (b-d) Inversion results of the checkerboard models located at depths of 520-660 km (b), 660-900 km (c), and 520-660 km and 660-900 km (d). In all the models, the anomaly surrounded by BOU, TUC, DLR and DAL, analogous to anomaly **W**, could be recovered rather well. Variables $\boldsymbol{\sigma}$ and $\boldsymbol{\sigma_0}$ are the conductivities of the inverted and reference models, respectively.

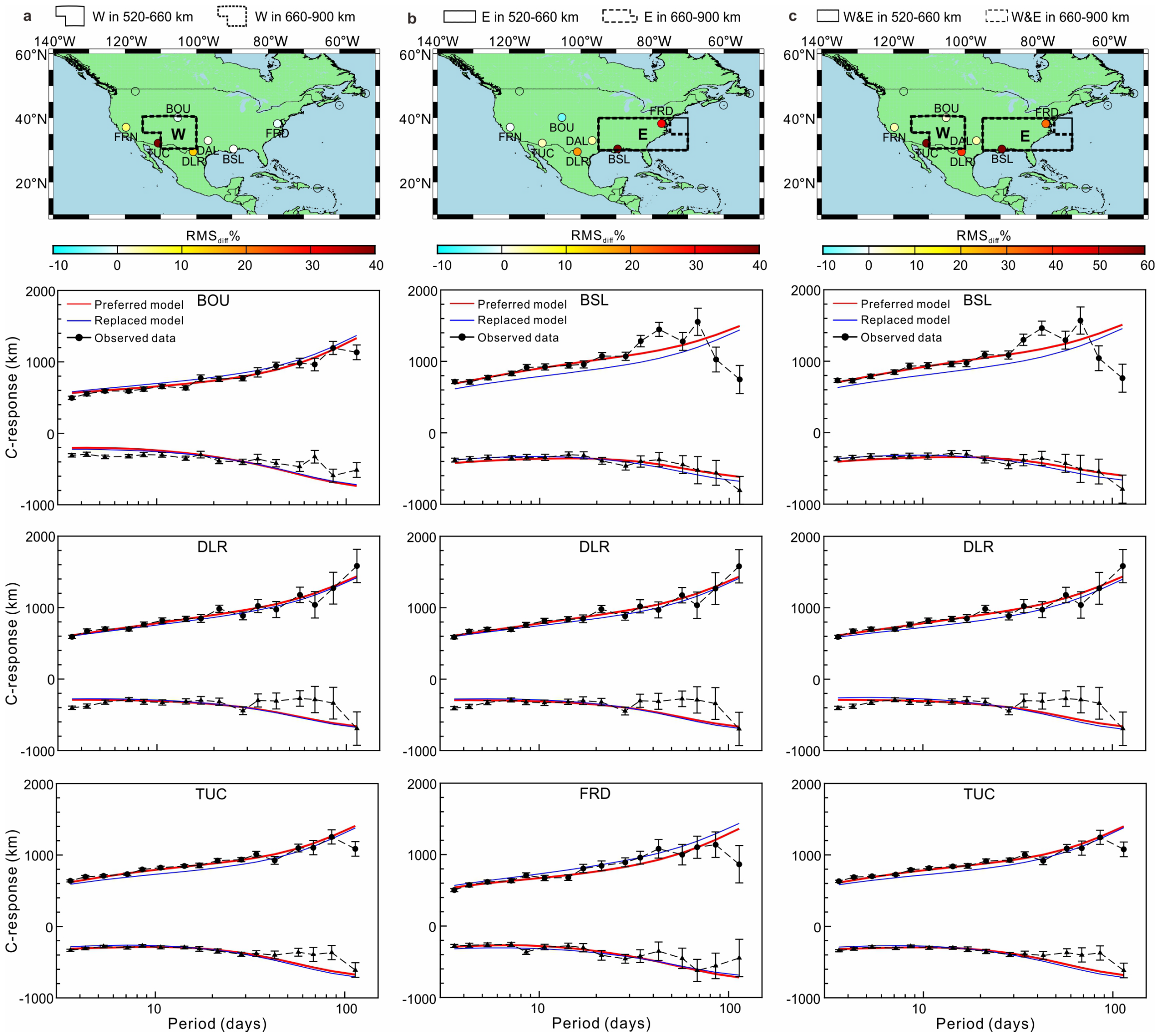

Figure S6. Robustness tests for anomaly W and E. (a) The conductivity of anomaly W, E and W & E (polygon in solid line and rectangle in dashed line) is replaced by the conductivity of the starting model. Different colors at the station indicate the change in the RMS error in the unit of percent. Curves are the changes in the *C*-responses over representative stations before and after model changes.

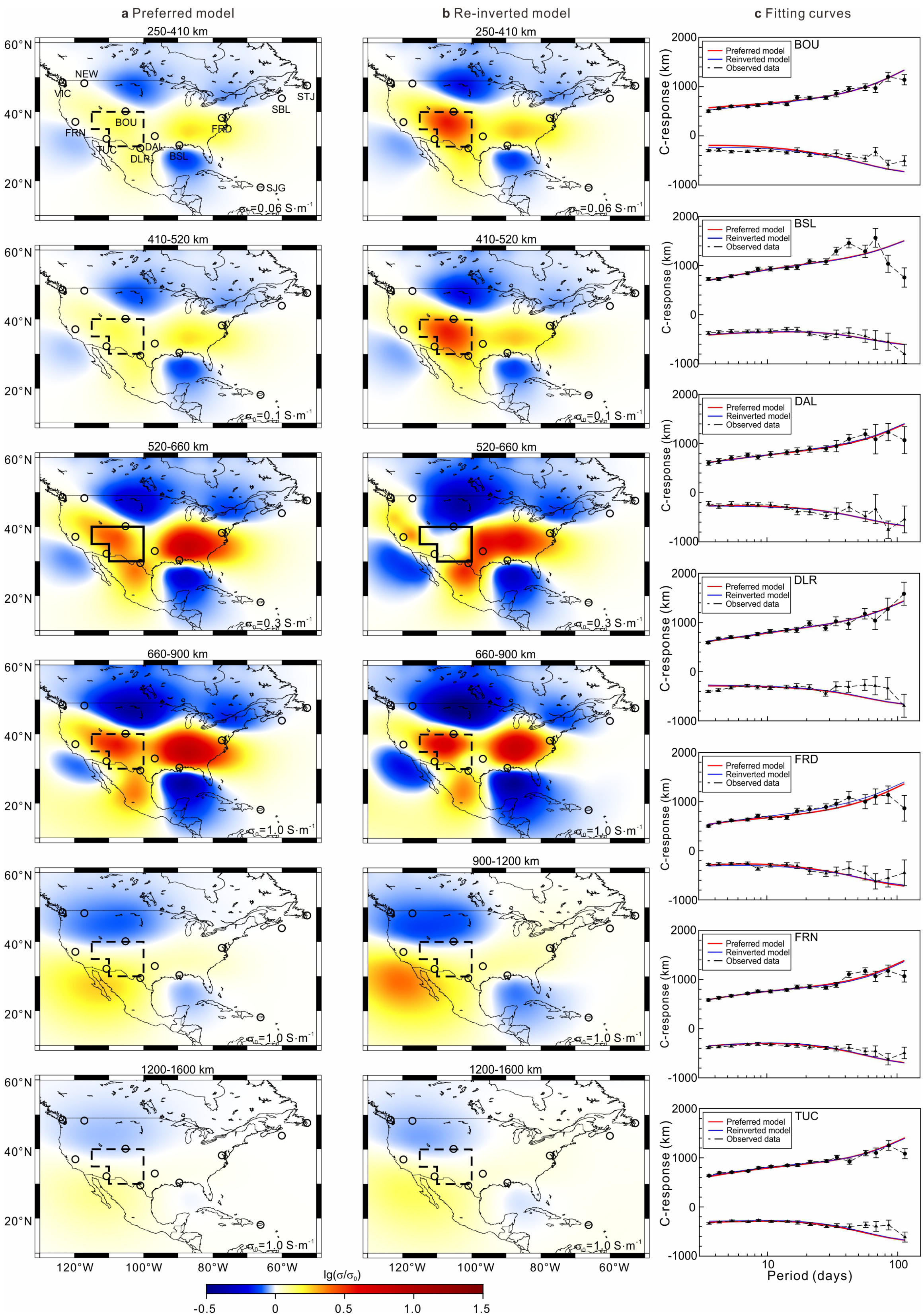

a Preferred model
b Re-inverted model
c Fitting curves
250-410 km
410-520 km
520-660 km
660-900 km
900-1200 km
1200-1600 km
NEW
VIC
STJ
SBL
BOU
FRN
TUC
DAL
DLR
BSL
FRD
SJG
60°N
40°N
20°N
120°W
100°W
80°W
60°W
σ0=0.06 S·m-1
σ0=0.1 S·m-1
σ0=0.3 S·m-1
σ0=1.0 S·m-1
lg(σ/σ0)
-0.5
0
0.5
1.0
1.5
Preferred model
Reinverted model
Observed data
BOU
BSL
DAL
DLR
FRD
FRN
TUC
C-response (km)
2000
1000
0
-1000
10
100
Period (days)

Figure S7. Compare of inversion results. (a) preferred inversion result, (b) result of inversion in which the conductivity of upper anomaly W (520-660 km, indicated by the black polygon) is returned to the initial value and fixed in inversion. (c) Fitting curves of responses of models in (a) and (b). Variables $\boldsymbol{\sigma}$ and $\boldsymbol{\sigma_0}$ are the conductivities of the inverted and reference models, respectively. The model in block mode is illustrated in continuous variation using the interpolation strategy of GMT (https://www.generic-mapping-tools.org/).

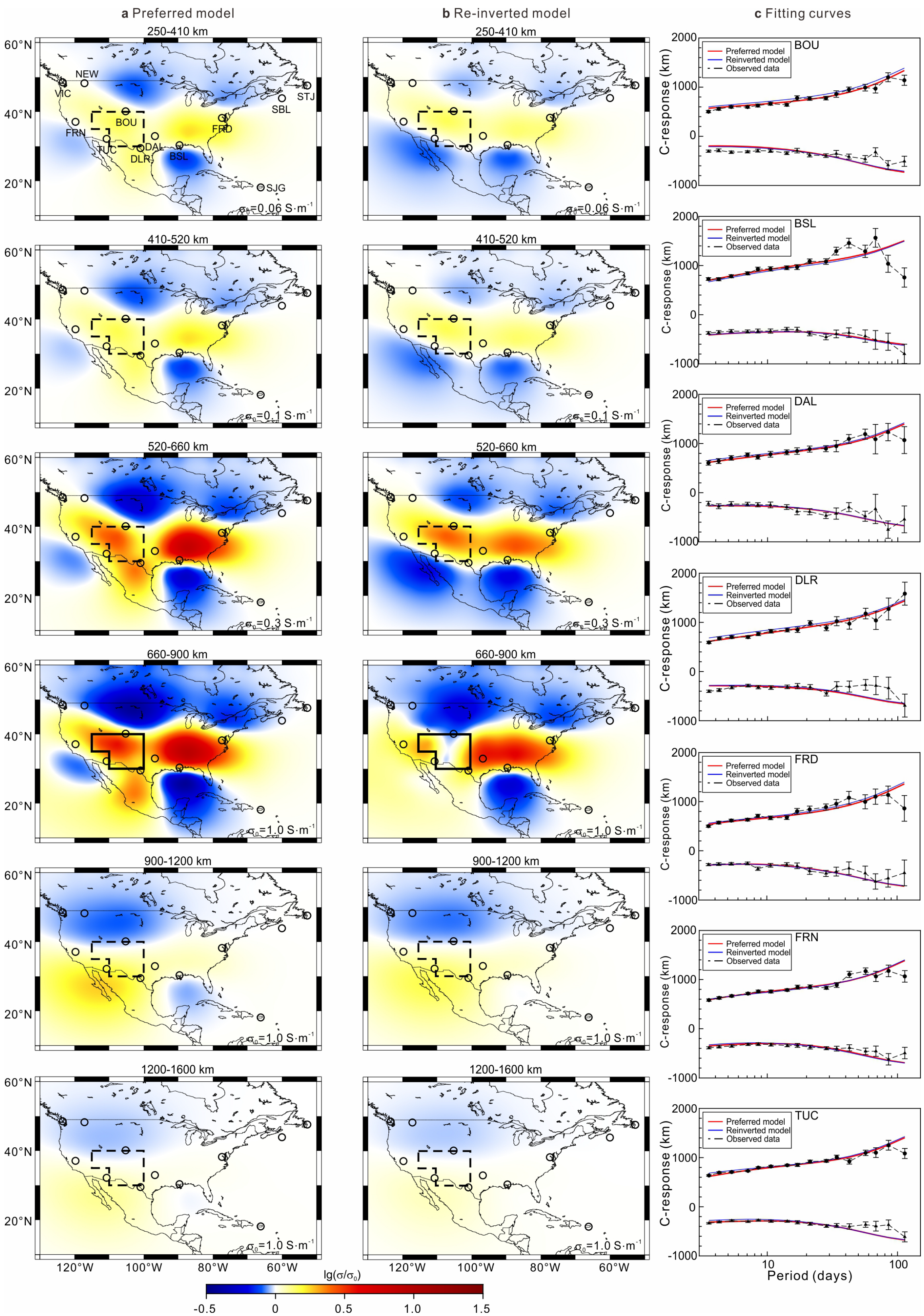
a Preferred model
b Re-inverted model
c Fitting curves
250-410 km
410-520 km
520-660 km
660-900 km
900-1200 km
1200-1600 km
NEW
VIC
STJ
SBL
BOU
FRN
TUC
DAL
DLR
BSL
FRD
SJG
60°N
40°N
20°N
120°W
100°W
80°W
60°W
σ0=0.06 S·m-1
σ0=0.1 S·m-1
σ0=0.3 S·m-1
σ0=1.0 S·m-1
lg(σ/σ0)
-0.5
0
0.5
1.0
1.5
Preferred model
Reinverted model
Observed data
BOU
BSL
DAL
DLR
FRD
FRN
TUC
C-response (km)
2000
1000
0
-1000
10
100
Period (days)

Figure S8. Compare of inversion results. (a) preferred inversion result, (b) result of inversion in which the conductivity of upper anomaly W (660-900 km, indicated by the black polygon) is returned to the initial value and fixed in inversion. (c) Fitting curves of responses of models in (a) and (b). Variables $\boldsymbol{\sigma}$ and $\boldsymbol{\sigma_0}$ are the conductivities of the inverted and reference models, respectively.

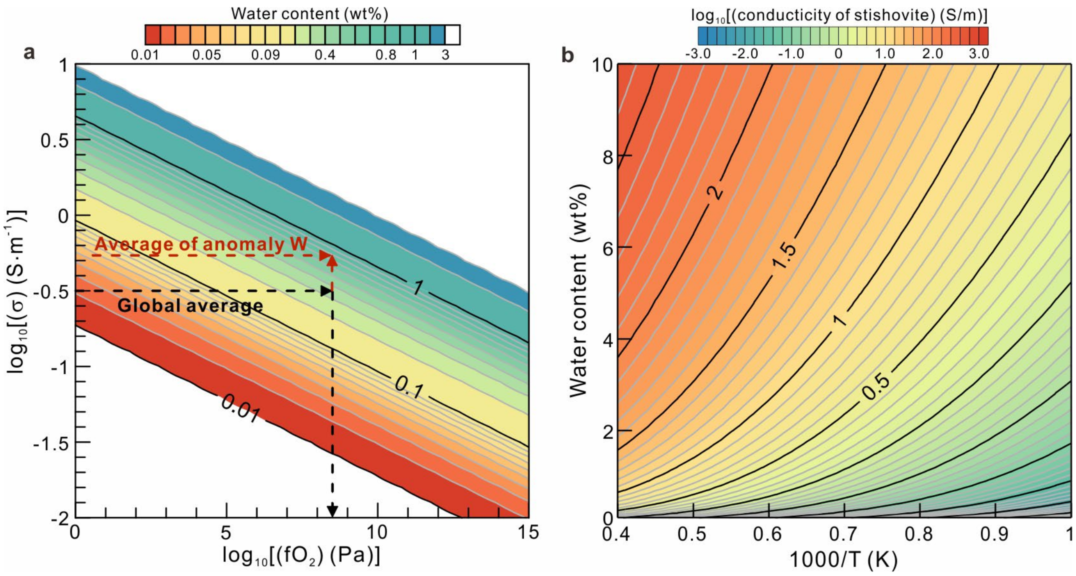

Supplementary Figure S9. Conductivity models for mantle mineral (ringwoodite and stishovite). (a) Electrical conductivity (σ) of ringwoodite as a function of oxygen fugacity (fO_2) and water content (Karato, 2011). Here, pressure is 21 GPa and temperature is 1848 K (Karato, 2011), corresponding to 600 km depth (near the middle of lower MTZ). The global average electrical conductivity is from ref (Kelbert et al., 2009). To estimate water content from conductivity, oxygen fugacity should be predefined. However, oxygen fugacity depends on temperature and pressure (Shofner et al., 2016). Here, it can be constrained to be ~$10^{8.5}$ Pa from the average global electrical conductivity (~0.3 S/m) and water content (0.35 wt%) in the MTZ (Kelbert et al., 2009). From this oxygen fugacity, ringwoodite is required to contain about 0.8 wt.% water in order to reproduce the conductivity of anomaly W (~0.6 S/m). (b) The variation in electrical conductivity of stishovite with reciprocal temperature and water content (Yoshino et al., 2014).

Supplementary References

Avdeev, D., and Avdeeva, A., 2009, 3D magnetotelluric inversion using a limited-memory quasi-Newton optimization: Geophysics, v. 74, doi:10.1190/1.3114023.

Banks, R.J., 1969, Geomagnetic Variations and the Electrical Conductivity of the Upper Mantle: Geophysical Journal of the Royal Astronomical Society, v. 17, p. 457–487, doi:10.1111/j.1365-246X.1969.tb00252.x.

Burd, A.I., Booker, J.R., Mackie, R., Favetto, A., and Pomposiello, M.C., 2014, Three-dimensional electrical conductivity in the mantle beneath the Payún Matrú Volcanic Field in the Andean backarc of Argentina near 36.5°S: Evidence for decapitation of a mantle plume by resurgent upper mantle shear during slab steepening: Geophysical Journal International, v. 198, p. 812–827, doi:10.1093/gji/ggu145.

Chave, A.D., and Thomson, D.J., 2004, Bounded influence magnetotelluric response function estimation: Geophysical Journal International, v. 157, p. 988–1006, doi:10.1111/j.1365-246X.2004.02203.x.

Farquharson, C.G., 2008, Constructing piecewise-constant models in multidimensional minimum-structure inversions: Geophysics, v. 73, p. K1–K9.

Hashin, Z., and Shtrikman, S., 1962, A Variational approach to the theory of the effective magnetic permeability of multiphase materials: Journal of Applied Physics, v. 33, p. 3125–3131, doi:10.1063/1.1728579.

Karato, S.I., 2011, Water distribution across the mantle transition zone and its implications for global material circulation: Earth and Planetary Science Letters, v. 301, p. 413–423, doi:10.1016/j.epsl.2010.11.038.

Karato, S., and Wang, D., 2013, Electrical Conductivity of Minerals, *in* Karato, S.-I. ed., Physics and Chemistry of the Deep Earth, John Wiley & Sons, Ltd, p. 145–182.

Kelbert, A., Schultz, A., and Egbert, G., 2009, Global electromagnetic induction constraints on transition-zone water content variations: Nature, v. 460, p. 1003–1006, doi:10.1038/nature08257.

Kuvshinov, A. V., 2002, Electromagnetic induction in the oceans and the anomalous behaviour of coastal *C*-responses for periods up to 20 days: Geophysical Research Letters, v. 29, p. 12–15, doi:10.1029/2001gl014409.

Kuvshinov, A., and Semenov, A., 2012, Global 3-D imaging of mantle electrical conductivity based on inversion of observatory *C*-responses-I. An approach and its verification: Geophysical Journal International, v. 189, p. 1335–1352, doi:10.1111/j.1365-246X.2011.05349.x.

Li, S., Weng, A., Zhang, Y., Schultz, A., Li, Y., Tang, Y., Zou, Z., and Zhou, Z., 2020, Evidence of Bermuda hot and wet upwelling from novel three-dimensional global mantle electrical conductivity image: Geochemistry, Geophysics, Geosystems, v. 21, doi:10.1029/2020GC009016.

Lin, Y., Hu, Q., Meng, Y., Walter, M., and Mao, H.-K., 2019, Evidence for the stability of ultrahydrous stishovite in Earth's lower mantle: Proceedings of the National

Academy of Sciences of the United States of America, v. 17, doi:10.1073/pnas.1914295117/-/DCSupplemental.

Manthilake, G., Schiavi, F., Zhao, C., Mookherjee, M., Bouhifd, M.A., and Jouffret, L., 2020, The Electrical Conductivity of Liebermannite: Implications for Water Transport Into the Earth's Lower Mantle: Journal of Geophysical Research: Solid Earth, v. 125, doi:10.1029/2020JB020094.

Menke, W., 1984, Geophysical Data Analysis: Discrete Inverse Theory: Orlando, Academi C Press , INC .

Ni, H., Keppler, H., and Behrens, H., 2011, Electrical conductivity of hydrous basaltic melts: Implications for partial melting in the upper mantle: Contributions to Mineralogy and Petrology, v. 162, p. 637–650, doi:10.1007/s00410-011-0617-4.

Semenov, A., and Kuvshinov, A., 2012, Global 3-D imaging of mantle conductivity based on inversion of observatory *C*-responses-II. Data analysis and results: Geophysical Journal International, v. 191, p. 965–992, doi:10.1111/j.1365-246X.2012.05665.x.

Shofner, G.A., Campbell, A.J., Danielson, L.R., Righter, K., Fischer, R.A., Wang, Y., and Prakapenka, V., 2016, The W-WO2 oxygen fugacity buffer (WWO) at high pressure and temperature: Implications for fO2 buffering and metal-silicate partitioning: American Mineralogist, v. 101, p. 211–221, doi:10.2138/am-2016-5328.

Sinmyo, R., Pesce, G., Greenberg, E., McCammon, C., and Dubrovinsky, L., 2014, Lower mantle electrical conductivity based on measurements of Al, Fe-bearing perovskite under lower mantle conditions: Earth and Planetary Science Letters, v. 393, p. 165–172, doi:10.1016/j.epsl.2014.02.049.

Uyeshima, M., and Schultz, A., 2000, Geoelectromagnetic induction in a heterogeneous sphere: A new three-dimensional forward solver using a conservative staggered-grid finite difference method: Geophysical Journal International, v. 140, p. 636–650, doi:10.1046/j.1365-246X.2000.00051.x.

Yoshino, T., 2010, Laboratory electrical conductivity measurement of mantle minerals: Surveys in Geophysics, v. 31, p. 163–206, doi:10.1007/s10712-009-9084-0.

Yoshino, T., Manthilake, G., Matsuzaki, T., and Katsura, T., 2008a, Dry mantle transition zone inferred from the conductivity of wadsleyite and ringwoodite: Nature, v. 451, p. 326–329, doi:10.1038/nature06427.

Yoshino, T., Nishi, M., Matsuzaki, T., Yamazaki, D., and Katsura, T., 2008b, Electrical conductivity of majorite garnet and its implications for electrical structure in the mantle transition zone: Physics of the Earth and Planetary Interiors, v. 170, p. 193–200, doi:10.1016/j.pepi.2008.04.009.

Yoshino, T., Shimojuku, A., and Li, D., 2014, Electrical conductivity of stishovite as a function of water content: Physics of the Earth and Planetary Interiors, v. 227, p. 48–54, doi:10.1016/j.pepi.2013.12.003.